Journal of Solid State Chemistry 181 (2008) 2565–2571

Contents lists available at ScienceDirect

Journal of Solid State Chemistry

journal homepage: www.elsevier.com/locate/jssc

Synthesis and characterization of a new four-layer Aurivillius phase $Bi_2SrNa_2Nb_4O_{15}$ and its protonated form

Zhenhua Liang [a,b], Kaibin Tang [a,b,*], Suyuan Zeng [b,a], Dong Wang [a,b], Tanwei Li [a], Huagui Zheng [b]

[a] Nanomaterial and Nanochemistry, Hefei National Laboratory for Physical Sciences at Microscale, University of Science and Technology of China, Hefei, Anhui 230026, PR China
[b] Department of Chemistry, University of Science and Technology of China, Hefei, Anhui 230026, PR China

ARTICLE INFO

Article history:
Received 16 April 2008
Received in revised form
9 June 2008
Accepted 10 June 2008
Available online 20 June 2008

Keywords:
Perovskite
Aurivillius
Powder X-ray diffraction
Protonated forms

ABSTRACT

A new four-layer Aurivillius phase $Bi_2SrNa_2Nb_4O_{15}$ has been synthesized by solid-state reaction of $Bi_2SrNb_2O_9$ and $NaNbO_3$ at 1100 °C. The detailed structure determination of $Bi_2SrNa_2Nb_4O_{15}$ performed by powder X-ray diffraction (XRD) shows that it crystallizes in the space group $I4/mmm$ [a∼3.9021(1) Å, c∼40.7554(10) Å]. Protonated form of $Bi_2SrNa_2Nb_4O_{15}$ was obtained by the substitution of bismuth oxide sheets with protons via acid treatment. The conversion into the protonated forms was achieved easily using 6 M HCl at room temperature. Preservation of the structure of the perovskite-like slabs and contraction in the c-axis were confirmed by X-ray analysis. The compositions of the resulting products were determined to be $H_{1.8}[Sr_{0.8}Bi_{0.2}Na_2Nb_4O_{13}]$ by X-ray fluorescence spectroscopy (XFS) and thermogravimetry.

1. Introduction

The Aurivillius phase, which was first discovered in 1949 [1–3], has a general formula $Bi_2O_2[A_{n-1}B_nO_{3n+1}]$, where the B-site cation resides in the interstitial site of an octahedron of oxygen anions, and the perovskite unit cell is built to form corner-sharing BO_6 octahedra that are connected through B–O–B linkages. The A-site cation fits in the large cavity at the center of eight corner-sharing BO_6 octahedra. $[A_{n-1}B_nO_{3n+1}]$ denotes the perovskite-like slabs derived by termination of the three-dimensional ABO_3 perovskite structure along the (100) axis, which are interleaved with $[Bi_2O_2]^{2+}$ fluorite-type layers, giving a characteristic layered structure.

Depending on the choice and stoichiometry of the A- and B-site cations, Aurivillius structure oxides can possess a wide variety of interesting properties. For example, $Bi_2SrTa_2O_9$ [4] and $Bi_{3.25}La_{0.75}Ti_3O_{12}$ [5] Aurivillius phases are in general noncentrosymmetric giving rise to ferroelectricity, nonvolatile memory and magnetoferroic properties [6]. Aurivillius phases have also found other properties or applications such as photoluminescence device [7], ion exchange and intercalation behavior [8–10], and the possibility of combining d^n and d^0 transition metal ions for the realization of multiferroic properties [11,12]. Since Kim has found that two-layer Aurivillius phase $Bi_2PbNb_2O_9$ was an excellent photocatalyst working under visible light in 2004 [13], there has been a growing interest in the study of Aurivillius phases which maybe potential photocatalytic materials in the future [14,15]. For example, a typical series of Aurivillius phases $Bi_2Mo_nO_{3n+3}$ ($n = 1$–3) had photocatalytic activity for O_2 evolution and could degrade organic compounds under visible-light irradiation [16–18]. Recently, there are several groups that have prepared one-layer Aurivillius phase Bi_2WO_6 nanoplates and nanoflowers to investigate their visible-light-driven photocatalytic activities [19–22]. These works revealed that Bi_2WO_6 could perform as an excellent photocatalytic material and solar-energy-conversion material.

Aurivillius phases with triple-layered perovskite-like slabs $[A_2B_3O_{10}]$, $Bi_2A'NaNb_3O_{12}$ ($A' = Sr$, Ca) and $Bi_2CaNaTa_3O_{12}$ have been reported by Sugahara and co-workers [23]. After that, Sugahara and co-workers have developed a novel method for obtaining protonated forms of layered perovskites derived from the Aurivillius phases through acid treatment of $Bi_2SrNaNb_3O_{12}$ and $Bi_2CaNaNb_3O_{12}$ [24] by the selective leaching of the bismuth oxide sheets and the corresponding introduction of protons for charge compensation. The overall reaction was the substitution of the bismuth oxide sheets with protons without changing the perovskite-like slab structure. Then they investigated the photocatalytic activities of triple-layered Aurivillius phases, $Bi_2A'NaNb_3O_{12}$ ($A' = Sr$, Ca) and $Bi_2CaNaTa_3O_{12}$, and of protonated forms prepared from these Aurivillius phases through selective

* Corresponding author at: Nanomaterial and Nanochemistry, Hefei National Laboratory for Physical Sciences at Microscale, University of Science and Technology of China, Hefei, Anhui 230026, PR China. Fax: +86 551 360 1791.
E-mail address: kbtang@ustc.edu.cn (K. Tang).

0022-4596/$ - see front matter © 2008 Elsevier Inc. All rights reserved.
doi:10.1016/j.jssc.2008.06.030

leaching of bismuth oxide sheets. They found that photocatalytic activity for H_2 evolution was greatly increased after selective leaching of the bismuth oxide sheets [14].

In this paper, we report a new successful example of four-layered Aurivillius phases $Bi_2SrNa_2Nb_4O_{15}$, which the *B*-sites were fully occupied by the niobium ions. Detailed powder X-ray diffraction (XRD) study of $Bi_2SrNa_2Nb_4O_{15}$ shows that this phase crystallizes in the space group *I*4/*mmm*. The conversion into the protonated forms was also investigated easily using 6 M HCl at room temperature. The structure and composition of the protonated forms as well as the mechanism of the conversion reaction will be compared and discussed with conventional proton-exchange reaction.

2. Experimental section

2.1. Preparation of $Bi_2SrNa_2Nb_4O_{15}$ samples

All reagents were analytically pure and used without further purification. Polycrystalline $Bi_2SrNa_2Nb_4O_{15}$ (BSNNO) powders were prepared by a solid-state reaction of a 1:2 mixture (total weight = 1.164 g) of $Bi_2SrNb_2O_9$ and $NaNbO_3$ at 1100 °C for 3 h (heating rate 10 °C/min), then the samples were cooled to room temperature in the furnace naturally. The calcination procedure was repeated another three times after grinding to ensure a complete reaction. $Bi_2SrNb_2O_9$ was prepared as reported in the literature [25] by reacting Bi_2O_3, $SrCO_3$ and Nb_2O_5 (total weight = 1.671 g) at 810 °C for 24 h and 900 °C for 24 h in air with a grinding in between (heating rate 10 °C/min). $NaNbO_3$ was prepared by reacting Na_2CO_3 and Nb_2O_5 (total weight = 0.944 g) at 1000 °C for 1 h in air (heating rate 10 °C/min). The purity of $Bi_2SrNb_2O_9$ and $NaNbO_3$ was confirmed by powder XRD.

2.2. Acid treatment of $Bi_2SrNa_2Nb_4O_{15}$

Typically, 1 g of BSNNO was treated with 200 cm^3 6 M HCl (M = mol/dm^3) and stirred at room temperature for 72 h to obtain acid-treated BSNNO as described elsewhere [24]. The acid-treated products $H_{1.8}[Bi_{0.2}Sr_{0.8}Na_2Nb_4O_{13}]$ (HSNNO) were collected by filtration. After being washed with deionized H_2O, the products were dried at 120 °C.

2.3. Sample characterization

Samples of $Bi_2SrNa_2Nb_4O_{15}$ were characterized by powder XRD recorded on a Philips X'Pert Pro Super diffractometer with Cu*K*α radiation ($\lambda = 1.54178$ Å) at room temperature (40 kV, 30 mA) in the angular range $5° < 2\theta < 110°$. The XRD data for indexing and cell-parameter calculation were collected in a continuous scan mode with a step size of 0.017°. The XRD patterns were analyzed by the Rietveld method using the FULLPROF program [26].

The size and the morphology of the product were observed on a SIRION FEI field emission scanning electronic microscope (FESEM) equipped with a GENESIS4000 energy-dispersive X-ray spectroscope. Thermal gravimetric analysis (TGA) of the protonated products was carried out on a Mettle Toledo TGA/SDTA 851e thermal analyzer at a heating rate of 10 °C/min from room temperature to 650 °C in the air. The cation ratios of the products were determined by an X-ray fluorescence spectrometer (XRF-1800 from Shimadzu). UV–vis diffuse reflectance spectrums (DRS) of the samples were measured by using a Hitachi U-3010 UV–vis spectrophotometer.

3. Results and discussion

3.1. Synthesis of $Bi_2SrNa_2Nb_4O_{15}$

The synthesis of four-layer perovskites that contain both Na^+ and Sr^{2+} in *B*-sites can be challenging, since Na^+ cations have smaller atomic radii ($r = 1.36$ Å) and smaller charge than those of Sr^{2+} cations ($r = 1.44$ Å) [27]. Likewise, there are often competing phases that are more stable than the desired layered perovskite. To successfully build four-layer Aurivillius structure, we employed two strategies. First, we synthesized the two-layer Aurivillius phase $Bi_2SrNb_2O_9$, which is more stable in high temperature. Second, we optimized a synthetic approach of iterative brief heating and regrinding that stabilized the target phase. Initial attempts to prepare the four-layer Aurivillius phase by direct heating stoichiometric mixtures of Na_2CO_3, Bi_2O_3, $SrCO_3$, and Nb_2O_5 at temperatures between 950 and 1100 °C failed because there were always many unknown impurities. In contrast, after a 3 h reaction time at 1100 °C, the desired phase was formed and the peaks corresponding to the four-layer Aurivillius structure were found in XRD pattern. When the sample was reground and heated again to 1100 °C for 3 h, the peaks corresponding to the desired phase increased. To ensure the desired four-layer Aurivillius phase was pure, the reaction was repeated for another two times. It is not yet clear why heating at 1100 °C for 4×3 h directly is significantly different from heating for the same length of time (12 h) in one step. It is possible that better mixing through intermediate grinding helps to direct the formation of the desired product.

3.2. Structure characterization of $Bi_2SrNa_2Nb_4O_{15}$

All peaks of the XRD pattern (in the angular range $7° < 2\theta < 50°$) could be indexed on a tetragonal cell [$a \sim 3.9021(1)$ Å, $c \sim 40.7554(10)$ Å] and the systematic absences showing body centering leading to an I—extinction symbol (Fig. 1). A starting model similar to $BaBi_4Ti_4O_{15}$ [28] in the space group *I*4/*mmm* was adopted to refine the structure. Initially, we suggested that all the Bi ions were only present in the bismuth oxide sheets. But the Rietveld refinement did not converge. Several early studies have indicated that the partial occupancy of Bi in the *A*-site is present in

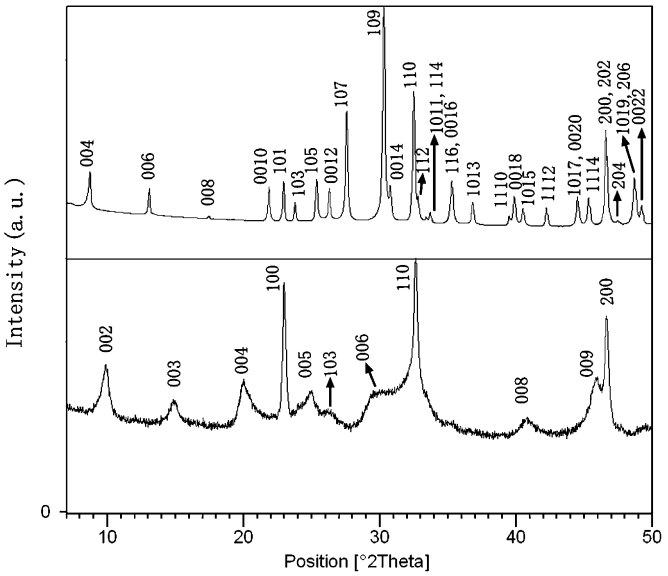

Fig. 1. XRD patterns of: (a) BSNNO and (b) the 120 °C dried product of BSNNO treated with 6 M HCl for 72 h.

$Bi_2SrNb_2O_9$ and $Bi_2SrNaNb_3O_{12}$ [23,24]. However, it would be really very hard to refine the structure because there were three different cations (Sr, Na and Bi), which were distributed in three sites of the crystal structure of $Bi_2SrNa_2Nb_4O_{15}$. Then we applied the method proposed by Joubert and co-workers [29] and there would be three parameters for occupancy of three cations in three sites in the refinement. Firstly, we refined all the parameters of cations while those of anions were excluded, and we found that the occupancies of Bi atoms in 2*a* sites were always negative. Thus we assumed that there were not any Bi atoms in 2*a* sites and then the refinement converged quickly.

The structure was refined by the Rietveld technique using all data of XRD above 10° (2θ) because of the high asymmetry of background at low angles as we can see from Fig. 1. For the refinement, with 39 parameters for 163 reflections, we found the conventional reliability factors, R_p, R_{wp}, R_{exp}, R_B and R_F to be 12.4%, 12.0%, 1.63%, 7.93% and 7.10%, respectively, unsatisfactory. The biggest error seemed to come from the 0 0 *l* reflections, always observed larger than calculated. Then we applied the March–Dollase option for correction in the FULLPROF program [26]. The result was greatly improved. Finally, we refined 40 parameters, and we got the best results (Table 1), R_p, R_{wp}, R_{exp}, R_B and R_F to be 9.53%, 9.12%, 1.62%, 4.74% and 5.06%, respectively (Fig. 2). While the heavy atoms are probably well located in our model, the X-ray powder data cannot allow a precise determination of the sodium and oxygen atom positions. As already encountered in such compounds, a small displacement of these oxygen atoms leading to a tilting of the octahedral could not be revealed by the powder XRD study. Indeed, Vlasenko and co-workers [30] have carried out structural analysis on $Bi_2CaNa_2Nb_4O_{15}$, based on X-ray powder diffraction experiments. Their work showed that tilting of the NbO_6 octahedra occurred in $Bi_2CaNa_2Nb_4O_{15}$ resulting in a lowering of symmetry to orthorhombic, $A2_1/am$. This titling is likely to be smaller in the present Sr sample and we could not obtain a stable refinement of the structure of $Bi_2SrNa_2Nb_4O_{15}$ using such a model.

A presentation of the $Bi_2SrNa_2Nb_4O_{15}$ structure is shown in Fig. 3. The structure consists of four layers of corner-sharing NbO_6 octahedra that run perpendicular to the *c*-axis; adjacent sets of layers are staggered as shown in Fig. 3. The octahedra forming the inner layer are less distorted with Nb–O distances ranging from 1.949(8) to 1.9880(16) Å (Table 2), which is typical for compounds

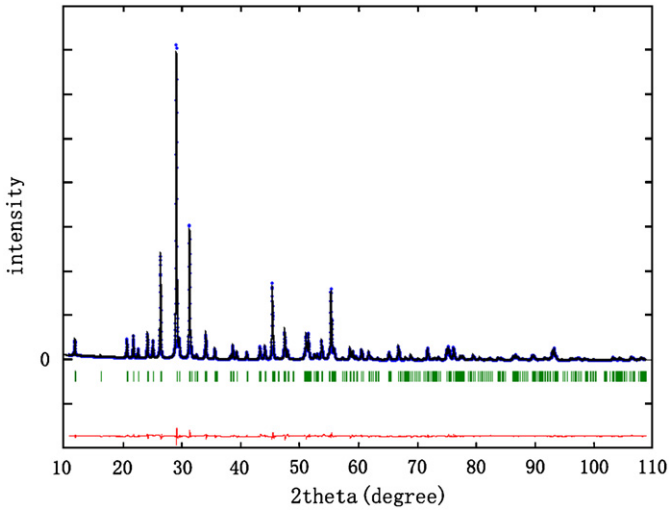

Fig. 2. Experimental (dotted line) calculated and difference (solid lines) powder X-ray diffraction patterns of $Bi_2SrNa_2Nb_4O_{15}$ after structural refinements in the space group *I*4/*mmm*. The vertical bars are the Bragg positions of the reflections in the space group *I*4/*mmm*.

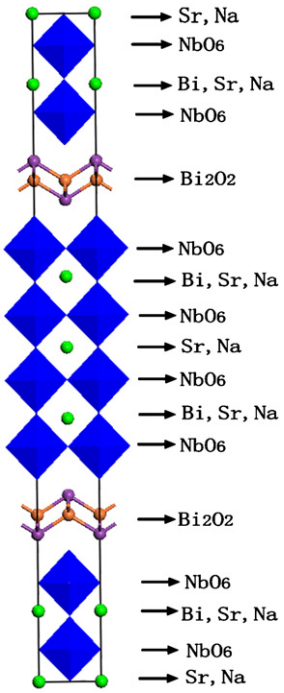

Fig. 3. Crystal structure of a four-layer Aurivillius phase $Bi_2SrNa_2Nb_4O_{15}$.

Table 1
The final refined atomic parameters for Rietveld powder X-ray refinement of $Bi_2SrNa_2Nb_4O_{15}$ in the space group *I*4/*mmm* ($Z=2$) with $a=3.9021(1)$ Å, $c=40.7554(10)$ Å

Atom	Site	*g*	*x*	*y*	*z*	*B* (Å^2)
Bi(1)	4*e*	0.82	0	0	0.22014(2)	1.878(31)
Sr(1)	4*e*	0.18	0	0	0.22014(2)	1.878(31)
Bi(2)	4*e*	0.18	0	0	0.10046(5)	2.001(87)
Sr(2)	4*e*	0.16	0	0	0.10046(5)	2.001(87)
Na(2)	4*e*	0.66	0	0	0.10046(5)	2.001(87)
Sr(3)	2*a*	0.16	0	0	0	1.937(165)
Na(3)	2*a*	0.34	0	0	0	1.937(165)
Nb(1)	4*e*	1	0	0	0.45122(3)	0.238(35)
Nb(2)	4*e*	1	0	0	0.35027(3)	0.565(40)
O(1)	2*b*	1	0	0	$\frac{1}{2}$	3.241(391)
O(2)	8*g*	1	0	$\frac{1}{2}$	0.04773(14)	4.040(226)
O(3)	4*e*	1	0	0	0.40343(21)	3.197(253)
O(4)	8*g*	1	0	$\frac{1}{2}$	0.14434(12)	2.498(187)
O(5)	4*e*	1	0	0	0.30781(25)	5.412(372)
O(6)	4*d*	1	0	$\frac{1}{2}$	$\frac{1}{4}$	5.900(353)

163 reflections and 40 parameters were used for refinement.
$R_p=9.53\%$, $R_{wp}=9.12\%$, $R_{exp}=1.62\%$, $R_B=4.74\%$, $R_F=5.06\%$. The preferential orientation parameter is $G1=0.9228(11)$.

Table 2
Selected interatomic distances (Å) for $Bi_2SrNa_2Nb_4O_{15}$

Sr(1)/Bi(1)–O(6) 1.9880(16) × 1	2.2995(4) × 4	Nb(1)–O(1)
Sr(1)/Bi(1)–O(5) 1.95153(14) × 4	2.985(5) × 4	Nb(1)–O(2)
Sr(2)/Bi(2)/Na(1)–O(4) 1.949(8) × 1	2.647(4) × 4	Nb(1)–O(3)
Sr(2)/Bi(2)/Na(1)–O(3) 2.165(8) × 1	2.7637(5) × 4	Nb(2)–O(3)
Sr(2)/Bi(2)/Na(1)–O(2) 1.9634(6) × 4	2.903(5) × 4	Nb(2)–O(4)
Na(2)/Sr(3)–O(2) 1.731(12) × 1	2.755(4) × 8	Nb(2)–O(5)
Na(2)/Sr(3)–O(1)	2.75922(4) × 4	

involving Nb(V). As it is well known in layered perovskites, the NbO_6 octahedra forming the outer layer of the slabs are characterized by off-centering of the Nb atoms, leading to four equal equatorial Nb–O distances within the perovskite layers [1.9634(6) Å], a short Nb–O bond toward the interlayer spacing [1.731(12) Å], and a long opposite Nb–O bond [2.165(8) Å]. Such a distortion is quite similar to that encountered in homologous niobates and tantalates where the niobium shows an out-of-plane distortion, moving away from the more positively charged strontium toward the bismuth oxide layer. Similar behavior has been observed in a number of d^0 systems containing niobium, tantalum, and titanium. This has been attributed to a second-order Jahn–Teller effect [31]. Concerning the bismuth oxide layer, the coordination tetrahedral pyramid involves the same four Bi–O bonds [2.2995(4) Å]. The Bi atoms in the bismuth oxide layer also have four longer bonds [2.985(5) Å] with the terminal oxygen atom O_5 of the nearest NbO_6 octahedron. These distances, as for the Sr (or Na)–O bonds [2.647(4)–2.903(5) Å], are in good agreement with the values in the literature.

A simple calculation based on the empirical expression $v_{ij} = \exp[(R_{ij} - d_{ij})/b]$, where R_{ij} and d_{ij} are the bond valence parameter and bond length [32], respectively, and b is commonly taken to be a universal constant equal to 0.37 Å [33], allows us to estimate valences in inorganic solids. The calculated bond valence

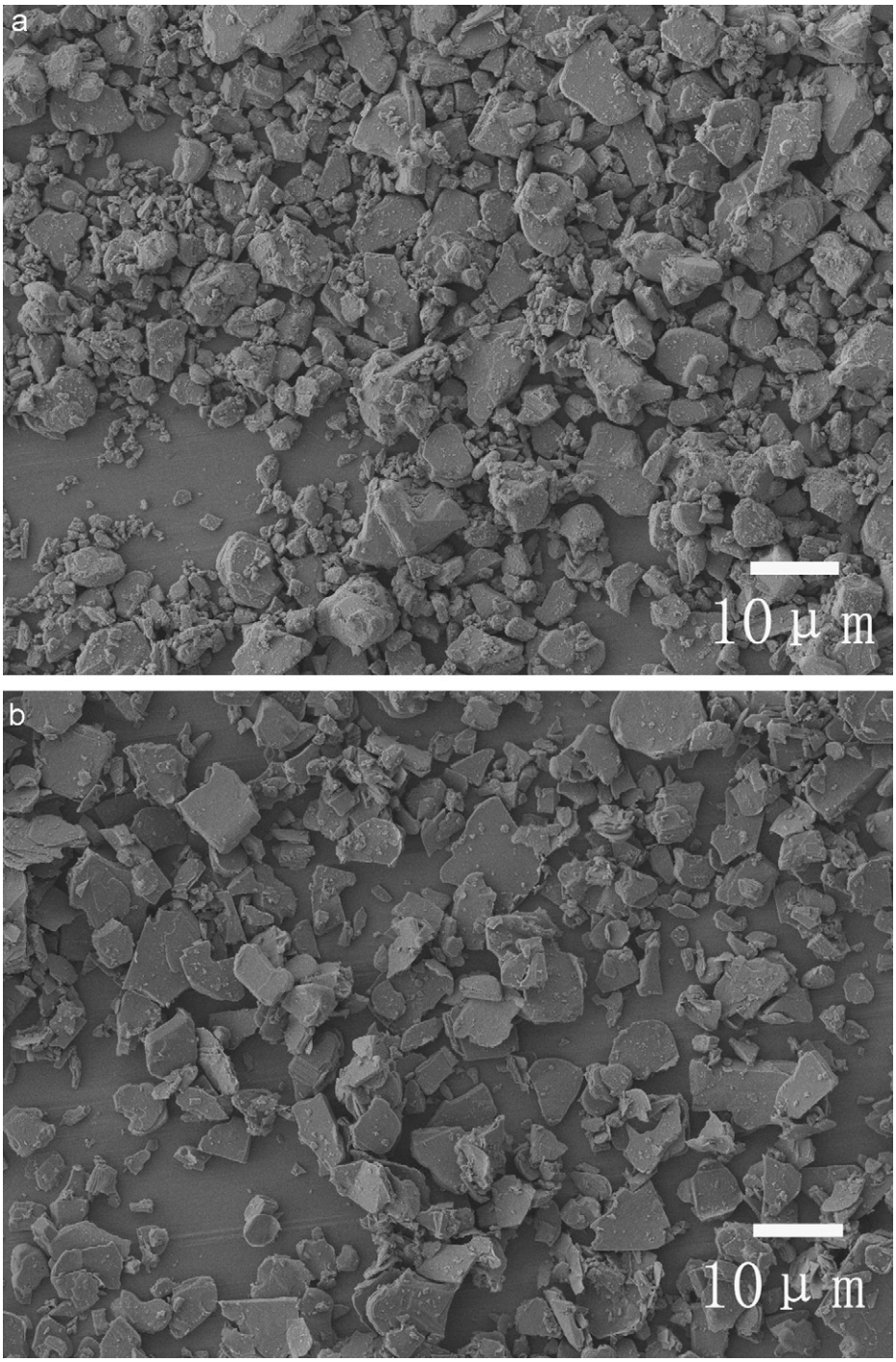

Fig. 4. SEM images of: (a) BSNNO and (b) the 120 °C dried product of BSNNO treated with 6 M HCl for 72 h.

sums for Nb1 and Nb2 in $Bi_2SrNa_2Nb_4O_{15}$ are 5.3 and 5.6, respectively, in reasonable agreement with the formal Nb oxidation state of +5.

Scanning electron micrographs of $Bi_2SrNa_2Nb_4O_{15}$ powders are shown in Fig. 4a. All $Bi_2SrNa_2Nb_4O_{15}$ powders are highly anisotropic with some irregular plate like morphology with diameters of 0.5–15 μm, indicating that there is really some platy preferential orientation in the XRD pattern.

3.3. Acid treatment of $Bi_2SrNa_2Nb_4O_{15}$

X-ray fluorescence spectroscopy (XFS) (Fig. 5) revealed the composition ratios of metals were Bi:Sr:Nb = 0.18:0.79:4.00 for HSNNO, indicating the selective leaching of Bi and the partial loss of Sr from BSNNO. These results, combined with the fact that (Bi+Sr):Nb = 0.97:4, suggest that partial disordering of cations (Bi and Sr) is present in the parent compound BSNN, similar to that reported for $Bi_2SrNaNb_3O_{12}$ [23].

The scanning electron micrograph of $H_{1.8}[Bi_{0.2}Sr_{0.8}Na_2Nb_4O_{13}]$ (Fig. 4b) shows that the morphology of the protonated products become more platy while preserving the platelet morphology of the precursors after ion-exchange reaction.

Fig. 6 shows the TG curve of $H_{1.8}[Bi_{0.2}Sr_{0.8}Na_2Nb_4O_{13}]$, the products obtained by treatment of BSNN with 6 M HCl for 72 h. The samples were dried at 120 °C to avoid the influence of adsorbed and/or interlayer water. The shape of the TG curves closely resembles those of protonated forms of layered perovskites obtained by conventional ion-exchange reactions with similar composition, such as $Bi_2SrNaNb_3O_{12}$ and $Bi_2CaNaNb_3O_{12}$ [24]. The observed mass loss of 2.2 mass% between ≈160 and ≈600 °C can be attributed to dehydroxylation, which is in excellent agreement with the anticipated mass loss of 2.2 mass% according to the following equation:

$$H_{1.8}[Bi_{0.2}Sr_{0.8}Na_2Nb_4O_{13}] \rightarrow Bi_{0.2}Sr_{0.8}Na_2Nb_4O_{12.1} + 0.9H_2O \quad (1)$$

Fig. 1 compares the XRD patterns of $Bi_2SrNa_2Nb_4O_{15}$ and its acid-treated products $H_{1.8}[Bi_{0.2}Sr_{0.8}Na_2Nb_4O_{13}]$. The structural transformation observed after acid treatment of BSNNO was similar to that observed after acid treatment of $Bi_2SrNaNb_3O_{12}$ [24]. Initially, the sharp diffraction peak at $2\theta = 22.9^\circ$ could be indexed as the (101) diffraction using a tetragonal cell with body-centered symmetry ($I4/mmm$) and $a \approx 3.89$ Å, $c \approx 35.49$ Å. However, it was hard to be explained while the other (hkl) peaks are much broader excepting those keen-edged ($hk0$) diffraction peaks. Therefore, the most reliable indexing of the XRD pattern for acid-treated BSNN was based on a primitive tetragonal cell with $a = 3.89 \pm 0.01$ Å and $c = 17.74 \pm 0.05$ Å. In this case, the sharp diffraction peak at $2\theta = 22.9^\circ$ could be reliably indexed as the (100) diffraction peak. The presence of the (00l) peaks at higher 2θ angles indicates the contraction of the basal spacing. The diffraction peaks of the perovskite sublattice (110) and (200) were observed at the same 2θ angles which revealed the retention of the structure along the ab plane, while the appearance of the (100) diffraction peak showed that the doubling of the c-axis observed in BSNNO does not occur in HSNNO. The broadness of the (hkl) ($l \neq 0$) peaks compared to that of the ($hk0$) peaks not only result from the platy morphology which can be seen in Fig. 4b, but also can be explained as the consequence of the stacking disorders present in acid-treated BSNNO.

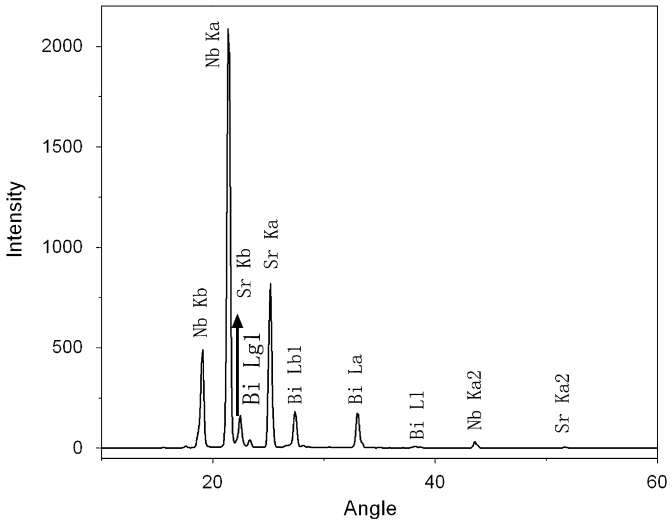

Fig. 5. X-ray fluorescence spectroscopy of the 120 °C dried product of BSNNO treated with 6 M HCl for 72 h.

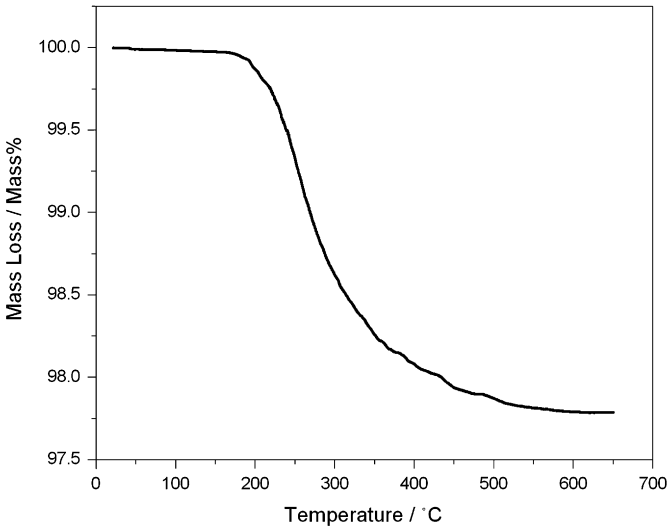

Fig. 6. TG curves of $H_{1.8}[Sr_{0.8}Bi_{0.2}Na_2Nb_4O_{13}]$.

For protonated forms of the layered perovskites, two types of stacking sequences of the perovskite-like slabs were reported: the simple stacking sequence without displacement [34] and the stacking sequence with a displacement by (a+b)/2 [35]. The unit cells of protonated phases possessing the simple stacking sequences contain only one perovskite-like slab which can be identified as P-type tetragonal cells while the relative displacement by (a+b)/2 leads to a doubling of the c-parameter, and the structures of the protonated forms were reported to possess I-type tetragonal cells. However, HREM observations of $H_{1.8}[Sr_{0.8}Bi_{0.2}Ta_2O_7]$ obtained by replacing the Bi_2O_2 layer with protons in the $n = 2$ Aurivillius phase $Bi_2SrTa_2O_9$, indicated the existence of two types of perovskite-like slab stacking [36]. In the case of $H_{1.8}[Bi_{0.2}Sr_{0.8}Na_2Nb_4O_{13}]$, the presence of the (100) peak in the XRD patterns (the (100) peak does not appear for tetragonal I-type cells) and the lack of doubling of the c-parameter suggest that the structure of protonated phase possesses a P-type cell as an average structure, disregarding the local stacking sequence of the perovskite-like slabs. The XRD results for acid-treated BSNNO indicate the presence of stacking disorders, which should complicate the accurate determination of the cell symmetry and stacking sequence of the perovskite-like slabs by the powder XRD patterns.

Accordingly, the overall reaction can be regarded as the replacement of the positively charged bismuth oxide sheets (containing Sr) with protons to compensate for the negatively charged perovskite-like slabs $\{(Bi_{1.8}Sr_{0.2}O_2)^{1.8+} \rightarrow 1.8xH^+)\}$. The reaction is schematically shown in Scheme 1. This should be

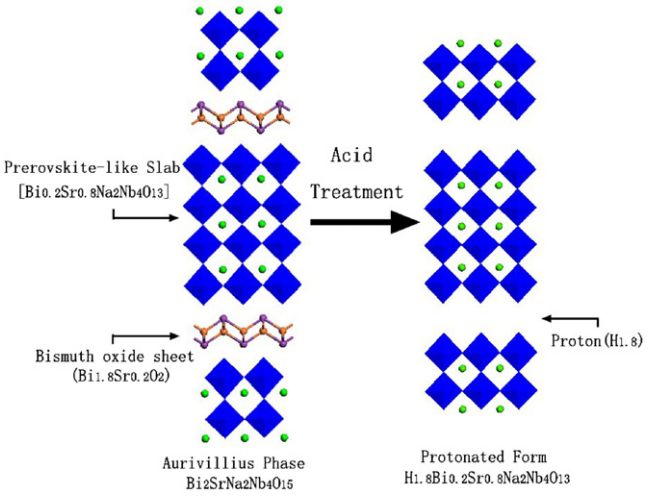

Scheme 1. Schematic representation of the conversion of the Aurivillius phase $Bi_2SrNa_2Nb_4O_{15}$ to the corresponding protonated forms of layered perovskite $H_{1.8}[Sr_{0.8}Bi_{0.2}Na_2Nb_4O_{13}]$.

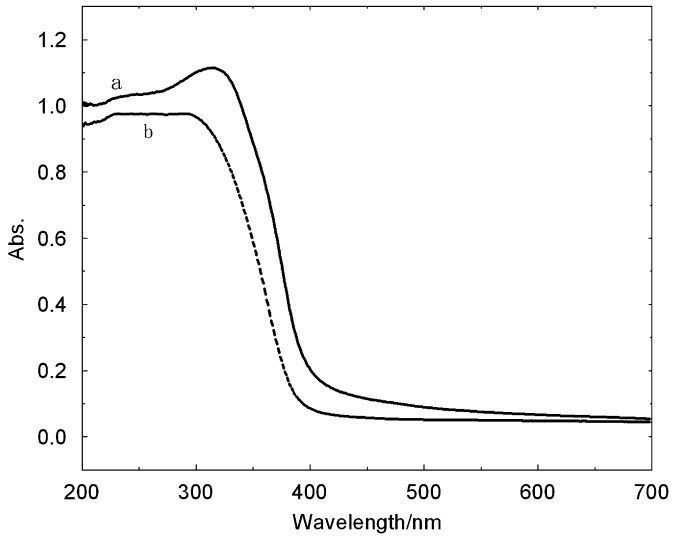

Fig. 7. UV–vis diffuse reflectance spectrum of: (a) $Bi_2SrNa_2Nb_4O_{15}$, the solid style curve and (b) $H_{1.8}[Sr_{0.8}Bi_{0.2}Na_2Nb_4O_{13}]$, the dashed-dotted style curve.

compared with the proton-exchange reaction ($M^+ \rightarrow H^+$) in ion-exchangeable layered perovskites.

3.4. *Photoabsorption properties of $Bi_2SrNa_2Nb_4O_{15}$ and its protonated form*

It is well known that light absorption by the material and the migration of the light-induced electrons and holes are the most key factors controlling a photocatalytic reaction, which is relevant to the electronic structural characteristics of the material [37,38]. The photoabsorption ability of $Bi_2SrNa_2Nb_4O_{15}$ and its acid-treated products $H_{1.8}[Sr_{0.8}Bi_{0.2}Na_2Nb_4O_{13}]$ was detected by UV–vis DRS, as shown in Fig. 7. $Bi_2SrNa_2Nb_4O_{15}$ presented the photo-absorption properties in the UV light region. The steep shape of the spectra indicated that the visible-light absorption was not due to the transition from the impurity level but was due to the bandgap transition. For a crystalline semiconductor, it was shown that the optical absorption near the band edge follows the

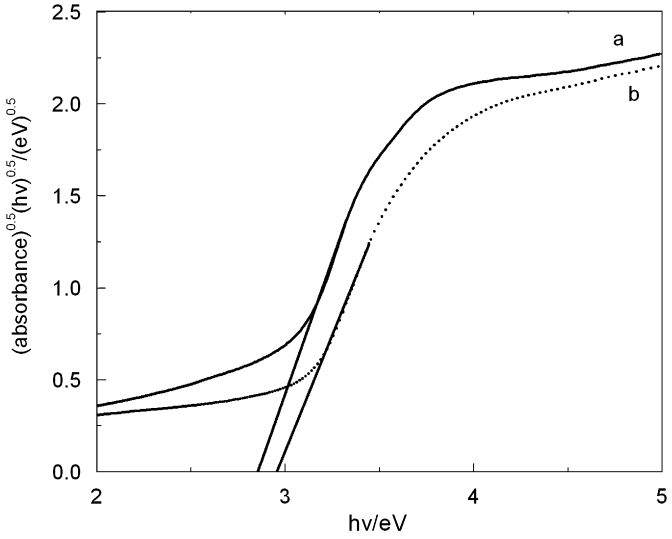

Fig. 8. The curve of $(Abs.)^{0.5}(h\nu)^{0.5}/(eV)^{0.5}$ plotted to $h\nu$/eV: (a) $Bi_2SrNa_2Nb_4O_{15}$, the solid style curve and (b) $H_{1.8}[Sr_{0.8}Bi_{0.2}Na_2Nb_4O_{13}]$, the dashed-dotted style curve.

equation $ah\nu = A(h\nu - E_g)^{n/2}$, where a, ν, E_g, and A are the absorption coefficient, the light frequency, the bandgap, and a constant, respectively. Among them, n decides the characteristics of the transition in a semiconductor. From the data in Fig. 8, the value of n for $Bi_2SrNa_2Nb_4O_{15}$ was 1 which is the same to the result of one-layered Aurivillius phase Bi_2WO_6 [39]. Upon acid treatment, a clear blue shift is shown in UV–vis diffuse reflectance spectra, and the bandgap increases correspondingly from 2.86 to 2.95 eV (Fig. 8). Similar blue shift was observed in the UV–vis diffuse reflectance spectra of the three-layered Aurivillius phase (from $Bi_2SrNaNb_3O_{12}$ to $H_{1.8}[Sr_{0.8}Bi_{0.2}NaNb_3O_{10}]$) [14]. Thus, this four-layered Aurivillius phase and its protonated form may have potential application in the fields of photocatalytic science and technology.

4. Conclusion

In summary, a new four-layer Aurivillius phase $Bi_2SrNa_2Nb_4O_{15}$ has been synthesized for the first time using solid-state reaction. The $Bi_2SrNa_2Nb_4O_{15}$ powders crystallize in the space group $I4/mmm$ [$a \sim 3.9021(1)$ Å, $c \sim 40.7554(10)$ Å]. Protonated form of $Bi_2SrNa_2Nb_4O_{15}$ was obtained by the substitution of bismuth oxide sheets with protons via acid treatment. The conversion into the protonated forms was achieved easily using 6 M HCl at room temperature. Preservation of the structure of the perovskite-like slabs and contraction in the c-axis were confirmed by X-ray analysis. The compositions of the resulting products were determined to be $H_{1.8}[Sr_{0.8}Bi_{0.2}Na_2Nb_4O_{13}]$ by XFS and thermo-gravimetry. UV–vis diffuse reflection spectra of the prepared $Bi_2SrNa_2Nb_4O_{15}$ and its acid-treated products indicate that they had absorption in the UV region. This work could be of great importance in extending the potential applications of $Bi_2SrNa_2Nb_4O_{15}$ and its acid-treated products.

Acknowledgments

Financial support by the National Natural Science Foundation of China (no. 20621061), the 973 Projects of China and the Program for New Century Excellent Talents in university (NCET) are gratefully acknowledged.

References

[1] B. Aurivillius, Ark. Kemi 1 (1949) 463–480.
[2] B. Aurivillius, Ark. Kemi 1 (1949) 499–512.
[3] B. Aurivillius, Ark. Kemi 2 (1950) 519–527.
[4] C. A-Paz de Araujo, J.D. Cuchiarom, L.D. McMillan, M.C. Scott, J.F. Scott, Nature 374 (1995) 627–629.
[5] B.H. Park, B.S. Kang, S.D. Bu, T.W. Noh, J. Lee, W. Jo, Nature 401 (1999) 682–684.
[6] A. Kingon, Nature 401 (1999) 658–659.
[7] S. Ida, C. Ogata, U. Unal, K. Izawa, T. Inoue, O. Altuntasoglu, Y. Matsumoto, J. Am. Chem. Soc. 129 (2007) 8956–8957.
[8] R.E. Schaak, T.E. Mallouk, Chem. Commun. (2002) 706–707.
[9] M. Kudo, H. Ohkawa, W. Sugimoto, N. Kumada, Z. Liu, O. Terasaki, Y. Sugahara, Inorg. Chem. 42 (2003) 4479–4484.
[10] S. Taharaa, A. Shimadaa, N. Kumadab, Y. Sugahara, J. Solid State Chem. 180 (2007) 2517–2524.
[11] E.E. McCabe, C. Greaves, J. Mater. Chem. 15 (2005) 177–182.
[12] N.A. Hill, J. Phys. Chem. B 104 (2000) 6694–6709.
[13] H.G. Kim, D.W. Hwang, J.S. Lee, J. Am. Chem. Soc. 126 (2004) 8912–8913.
[14] M. Kudo, S. Tsuzuki, K. Katsumata, A. Yasumori, Y. Sugahara, Chem. Phys. Lett. 393 (2004) 12–16.
[15] H.G. Kim, O.S. Becker, J.S. Jang, S.M. Ji, P.H. Borse, J.S. Lee, J. Solid State Chem. 179 (2006) 1214–1218.
[16] J.C. Jung, H. Lee, H. Kim, Y.M. Chung, T.J. Kim, S.J. Lee, S.H. Oh, Y.S. Kim, I.K. Song, J. Mol. Catal. A: Chem. 271 (2007) 261–265.
[17] Y. Shimodaira, H. Kato, H. Kobayashi, A. Kudo, J. Phys. Chem. B 110 (2006) 17790–17797.
[18] A.M. la Cruz, S.O. Alfaro, E.L. Cuellar, U.O. Mendez, Catal. Today 129 (2007) 194–199.
[19] L.S. Zhang, W.Z. Wang, L. Zhou, H.L. Xu, Small 3 (2007) 1618–1625.
[20] L.S. Zhang, W.Z. Wang, Z.G. Chen, L. Zhou, H.L. Xu, W. Zhu, J. Mater. Chem. 17 (2007) 2526–2532.
[21] H.B. Fu, L.W. Zhang, W.Q. Yao, Y.F. Zhu, Appl. Catal. B: Environ. 66 (2006) 100–110.
[22] J. Wu, F. Duan, Y. Zheng, Y. Xie, J. Phys. Chem. C 111 (2007) 12866–12871.
[23] W. Sugimoto, M. Shirata, Y. Sugahara, K. Kuroda, J. Am. Chem. Soc. 121 (1999) 11601–11602.
[24] W. Sugimoto, M. Shirata, K. Kuroda, Y. Sugahara, Chem. Mater. 14 (2002) 2946–2952.
[25] Ismunandar, B.J. Kennedy, Gunawan, Marsongkohadi, J. Solid State Chem. 126 (1996) 135–141.
[26] J. Rodriguez-Carvajal, FULLPROF program: Rietveld pattern matching analysis of powder patterns, ILL Grenoble, 1990.
[27] R.D. Shannon, Acta Crystallogr. A 32 (1976) 751–767.
[28] G. Nalini, T.N. Guru Row, Bull. Mater. Sci. 25 (2002) 275–281.
[29] J.M. Joubert, R. Cerny, M. Latroche, A. Percheron-Gugan, K. Yvon, J. Appl. Crystallogr. 31 (1998) 327–332.
[30] V.G. Vlasenko, A.T. Shovaev, D.S. Drannikov, Powder Diffraction 20 (2005) 1–6.
[31] N.S.P. Bhuvanesh, J. Gopalakrishnan, J. Mater. Chem. 7 (1997) 2297–2306.
[32] N.E. Brese, M. O'Keeffe, Acta Crystallogr. B 47 (1991) 192–197.
[33] I.D. Brown, D. Altermatt, Acta Crystallogr. B 41 (1985) 244–247.
[34] P.J. Ollivier, T.E. Mallouk, Chem. Mater. 10 (1998) 2585–2587.
[35] Y. Tsunoda, M. Shirata, W. Sugimoto, Z. Liu, O. Terasaki, Y. Sugahara, K. Kuroda, Inorg. Chem. 40 (2001) 5768–5771.
[36] N.S.P. Bhuvanesh, M.P. Crosnier-Lopez, H. Duroy, J.L. Fourquet, J. Mater. Chem. 10 (2000) 1685–1692.
[37] J.W. Tang, Z.G. Zou, J.H. Ye, Angew. Chem. Int. Ed. 43 (2004) 4463–4466.
[38] J.W. Tang, Z.G. Zou, J.H. Ye, Chem. Mater. 16 (2004) 1644–1649.
[39] C. Zhang, Y.F. Zhu, Chem. Mater. 17 (2005) 3537–3545.